JACS Au
AN OPEN ACCESS JOURNAL OF THE AMERICAN CHEMICAL SOCIETY

pubs.acs.org/jacsau

Article

Activity of Cu−Al−Oxo Extra-Framework Clusters for Selective Methane Oxidation on Cu-Exchanged Zeolites

Insu Lee,[†] Mal-Soon Lee,*[,†] Lei Tao, Takaaki Ikuno, Rachit Khare, Andreas Jentys, Thomas Huthwelker, Camelia N. Borca, Aleksandr Kalinko, Oliver Y. Gutiérrez, Niri Govind, John L. Fulton, Jian Zhi Hu, Vassiliki-Alexandra Glezakou, Roger Rousseau, Maricruz Sanchez-Sanchez,* and Johannes A. Lercher*

Cite This: *JACS Au* 2021, 1, 1412−1421

Read Online

ACCESS | Metrics & More | Article Recommendations | Supporting Information

ABSTRACT: Cu-zeolites are able to directly convert methane to methanol via a three-step process using O_2 as oxidant. Among the different zeolite topologies, Cu-exchanged mordenite (MOR) shows the highest methanol yields, attributed to a preferential formation of active Cu−oxo species in its 8-MR pores. The presence of extra-framework or partially detached Al species entrained in the micropores of MOR leads to the formation of nearly homotopic redox active Cu−Al−oxo nanoclusters with the ability to activate CH_4. Studies of the activity of these sites together with characterization by ^{27}Al NMR and IR spectroscopy leads to the conclusion that the active species are located in the 8-MR side pockets of MOR, and it consists of two Cu ions and one Al linked by O. This Cu−Al−oxo cluster shows an activity per Cu in methane oxidation significantly higher than of any previously reported active Cu−oxo species. In order to determine unambiguously the structure of the active Cu−Al−oxo cluster, we combine experimental XANES of Cu K- and L-edges, Cu K-edge HERFD-XANES, and Cu K-edge EXAFS with TDDFT and AIMD-assisted simulations. Our results provide evidence of a $[Cu_2AlO_3]^{2+}$ cluster exchanged on MOR Al pairs that is able to oxidize up to two methane molecules per cluster at ambient pressure.

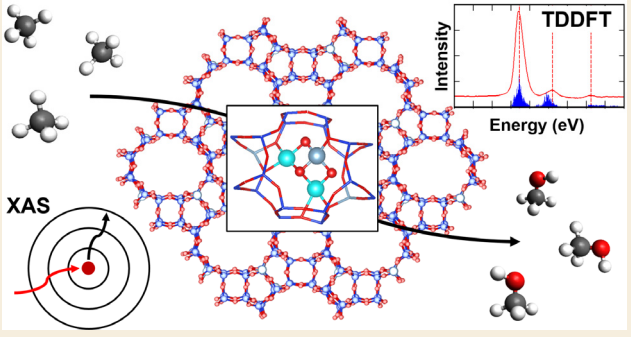

KEYWORDS: *Methane oxidation, Cu L_3-edge XANES, HERFD, TDDFT, zeolite, AIMD*

INTRODUCTION

Increased availability of light hydrocarbons from shale gas raised the interest in methane as feedstock for the petrochemical industry.[1] Currently, methane is mainly converted via synthesis gas to methanol, higher alcohols, and a range of hydrocarbons.[1,2] Despite the high maturity of these routes, a single-step transformation would have significant advantages, triggering substantial interest in the direct conversion of methane to methanol.[2−5]

Copper-exchanged zeolites have shown activity in the selective oxidation in repeatable single turnovers using O_2 as oxidant.[3,6,7] Grootheart et al. were the first to demonstrate this via a cyclic three-stage process, which is depicted schematically in Figure 1.[8] Among the variety of zeolite topologies, zeolite MOR, having straight 12-membered-ring (MR) channels and intersecting 8-MR side pockets, had the best utilization of copper.[3,6,9] Dimeric[10−15] and trimeric[16−19] Cu−oxo clusters have been proposed to be the main active sites. Al pairs in the 8-MR side pockets of MOR favor the formation and stabilization of such active Cu−oxo sites.[17,18,20,21] It has been established that each Cu−oxo cluster is able to oxidize one CH_4 at ambient pressure and up to two CH_4 at higher CH_4 chemical potentials.[22]

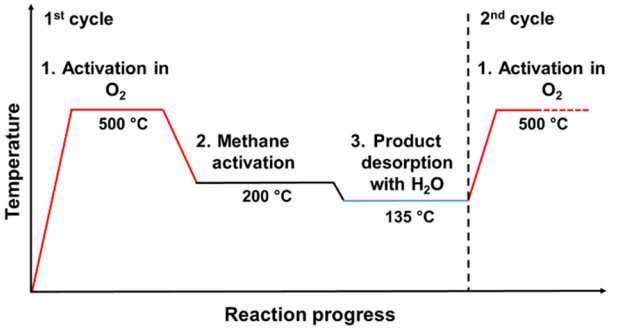

Figure 1. Scheme of the three stage reaction cycle for the conversion of methane to methanol over Cu-exchanged zeolites.

Received: May 5, 2021
Published: July 14, 2021

The fraction of Cu that can be stabilized as active Cu−oxo clusters in a zeolite depends on the concentration of Al in the zeolite lattice, its crystallographic position, the fraction of Al T sites among its next nearest neighbors, and the presence of other cations in the zeolite. Optimized ion-exchange protocols and the absence of cocations leads to high concentrations of active Cu−oxo sites.[17,18]

In the absence of other metal cations, Brønsted acidic zeolites undergo some dealumination, resulting in the formation of (partially detached) extra-framework Al (EFAl) species such as $Al(OH)_x$ (Al_xO_y).[23−27] These EFAl species influence Brønsted acid site (BAS)-catalyzed reactions.[28−32] A recent study by Dyballa et al. reported Cu-MOR materials with an increased activity in methane oxidation and associated it to the presence of higher concentrations of extra-framework aluminum.[33] However, it is unknown how the EFAl influence active Cu−oxo species.

In this work, we investigate the activity of methane oxidation to methanol by Cu−oxo species in MOR in the presence of EFAl. We report on a series of Cu-MOR with nearly 2× higher productivity per Cu atom than so far established for the best Cu-MOR materials (under 1 bar and stepwise mode).[14,16,17] This drastic increase in activity points to an intrinsically different Cu−oxo species.

Using NMR and IR spectroscopy, we report evidence of the interaction of Cu with extra-framework Al species in these highly active Cu-exchanged zeolites. To better understand the sites, the Cu-MOR samples were studied by a combination of X-ray absorption spectroscopies (XAS) and theory. High-energy-resolution-fluorescence-detected (HERFD) and X-ray absorption near-edge structure (XANES) of the Cu K-edge were used to define the nature and local geometry of Cu.[34] The combination of structural and chemical information derived from these measurements together with EXAFS of the Cu K- and Al K-edges of the Cu-MOR materials and Cu L-edge XANES is used to characterize the oxidation state of Cu together with highly specific information about bonding of the oxo ligands.[35] To complement and augment our experimental measurements, we have performed ground state spin-polarized density functional theory (DFT)-based ab initio molecular dynamics (AIMD) simulations and EXAFS and TDDFT-based XANES calculations.[36]

RESULTS AND DISCUSSION

Activity of Cu-MOR Catalysts Prepared under Controlled Conditions

We have measured the reactivity of two Cu-MOR series, denoted as Cu-MOR-A and Cu-MOR-B, in a typical three-stage reaction comprising of (1) high temperature activation of 500 °C in O_2, (2) exposure to methane at 200 °C and 1 bar, and (3) product desorption by steam treatment. In order to compare the relative reactivity of Cu-MOR samples, we define the Cu efficiency (Cu_{eff}) as the molar ratio of all converted CH_4 to the total amount of Cu present. Our previous reports agree well with those of other authors in reporting an upper limit of Cu_{eff} = 0.35 for Cu-MOR materials at 1 bar.[14,16,17,22,37] Only when the CH_4 chemical potential was significantly increased (by increasing P_{CH4} to 40 bar, for instance) it was possible to achieve higher Cu_{eff} values, in the range of 0.45−0.6.[14,22]

Here, we report an unusually high Cu_{eff} for Cu exchanged on a zeolite (H-MOR-B) that contains extra-framework aluminum (EFAl) at a different T-site position. For this highly active Cu-MOR zeolite series, an average Cu_{eff} of 0.58 was obtained at 1 bar for Cu loadings up to 300 μmol/g (Figure 2).[14,15,33]

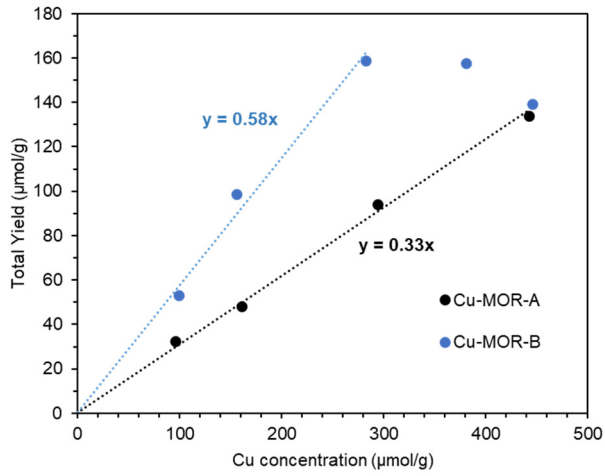

Figure 2. Yield of CH_4 oxidation on the Cu-MOR catalysts prepared from different parent H-MOR samples with different Cu loading of Cu-MOR-A and Cu-MOR-B series. Numerical values of the Cu_{eff} are given as $y = Cu_{eff}x$ for Cu-MOR-A (black) and Cu-MOR-B (blue). Activity tests were repeated three times on each catalyst and averaged values are reported.

Selectivities to MeOH and its dehydration product dimethyl ether/DME) were in the range of 65 to 85% (see Supporting Information, Figure S1) and activity was fully restored by the oxidative treatment at least for seven consecutive catalytic cycles (Figure S2). We include here for comparison the Cu-MOR-A series, showing consistently a Cu_{eff} of 0.33 and selectivities to MeOH + DME between 65 and 80% (Figure S1). Our previous work on this material allows us to firmly attribute the activity to the oxidation of one molecule of CH_4 by a $[Cu_3(\mu\text{-}O)_3]^{2+}$ cluster.[17] Characterization of these different Cu-MOR samples is used to elucidate the origin of the high efficiency achieved for the new material.

Characterization of Parent MOR-A and MOR-B Samples

The distribution of Al in the zeolite framework is an important parameter for the location of Cu^{2+} after ion exchange. Two next-nearest neighboring Al tetrahedra ("Al pairs") allows best to stabilize divalent cations.[38,39] The formation of dimeric and trimeric Cu−oxo clusters is proposed to occur on such paired Al sites.[14,15,17,40,41] The concentration of Al pairs in the parent H-MOR materials can be determined by aqueous Co^{2+} exchange.[38,39] Here we have employed two commercial zeolites, MOR-A and MOR-B, that only differ in their Al distribution, originated by differences in the zeolite synthesis parameters. Table S1 shows the concentrations of the Al pairs for H-MOR-A (63%) and H-MOR-B (66%). As the number of Al pairs is nearly identical, the concentration of exchange sites alone is, thus, ruled out as a reason for the higher Cu_{eff} of Cu-MOR-B.

The location of the ion exchange sites was determined from the IR spectra of adsorbed *n*-hexane and pyridine on the parent H-MOR samples. *n*-Hexane is only able to interact with BAS in the 12-MR channels (Figure S3).[17,42] Conversely, the more basic pyridine is protonated by all BAS in 12-MR and in the pore mouth of the 8-MR side pockets. Table 1 shows clearly that the concentration and location of BAS, as obtained by a

https://doi.org/10.1021/jacsau.1c00196
JACS Au 2021, 1, 1412−1421

Table 1. Quantification of Al Species and Their Distribution in the Parent H-MOR-A and H-MOR-B, by a Combination of Chemical Analysis, IR Spectroscopy of *n*-Hexane and Pyridine Adsorption, and ^{27}Al MAS NMR

	H-MOR-A	H-MOR-B
total Al[a] (μmol/g)	1440	1620
total BAS[b] (μmol/g)	1090[h]	1130
total EFAl[c] (μmol/g)	350	490
$BAS_{main\_channel}$[d] (μmol/g)	400[h]	419
$BAS_{side\text{-}pocket}$[d] (μmol/g)	690[h]	706
LAS_{Py} (μmol/g)[e]	260[h]	230
$EFAl_{inaccessible}$[f] (μmol/g)	90	260
$Al_{tetrahedral}$[g] (μmol/g)	1156	1290
$Al_{octahedral}$[g] (μmol/g)	284	330

[a]Total Al concentration determined by elemental analysis (AAS). [b]Total BAS concentration determined by elemental analysis after Na ion exchange of the parent H-MOR samples (assuming all H^+ are exchanged by Na^+). [c]Total EFAl concentration was determined by [total Al] − [total BAS]. [d]Concentration of BAS located in 12-MR and 8-MR, as determined by deconvolution of the IR band at 3600 cm^{-1} (Figure S3) after *n*-hexane adsorption. [e]Concentration of LAS accessible by pyridine, as determined by IR spectroscopy. [f]Concentration of EFAl located in the inaccessible bottom of 8-MR side pockets was determined by [total EFAl] − [LAS_{Py}]. [g]Based on ^{27}Al NMR. [h]Values as reported in ref 17.

combination of these probe molecules, are also similar for H-MOR-A and H-MOR-B. The location of the EFAl species is deduced from both pyridine adsorbed on Lewis acid sites and from the total Al concentration derived from the elemental analysis. If we assume that Lewis-coordinated pyridine adsorbs in a 1:1 ratio to Al atoms of extra-framework species, the inaccessible EFAl can be calculated as the total measured Al concentration minus the sum of all BAS (framework Al) and Lewis acid sites (LAS). While the total concentration of LAS determined by pyridine is similar for H-MOR-A and H-MOR-B (Table 1), the concentration of EFAl in H-MOR-B inaccessible to pyridine was significantly higher than in H-MOR-A. We hypothesize that this inaccessible EFAl is located near the bottom of the 8-MR side pockets.

^{27}Al MAS NMR spectra in Figure S4a show two peaks at 58 and 0 ppm, corresponding to tetrahedral and octahedral Al species.[33] The octahedral Al fraction was found to account for approximately 20% of Al for both parent H-MOR samples (Table 1). This concentration of octahedral Al determined by ^{27}Al MAS NMR is smaller than that determined from pyridine adsorption (Table 1), suggesting that some of the EFAl-related Lewis acid sites have tetrahedral coordinated Al.[43] It should be emphasized that H-MOR-B has about a 3× higher concentration of inaccessible EFAl than MOR-A.

Location of Exchanged Cu Species in Standard and Highly Active MOR

All samples in this study have more than 90% of Cu at ion exchange sites (determined by Na^+ back-exchange, see Table S2 in the SI). The preferred exchange sites for Cu^{2+} in H-MOR were determined by analysis of the decrease in intensity of the band of SiOHAl groups at 3600 cm^{-1} after Cu^{2+} ion exchange. This band consists of two contributions at 3612 and 3590 cm^{-1}, attributed to BAS in the 12-MR main channel and the 8-MR side pockets, respectively.[41] The preferred sites for ion-exchange in MOR are the more constrained 8-MR side pockets.[44] In Cu-MOR-A, the formation of the active trimeric Cu−oxo cluster was observed selectively at the pore mouth of the 8-MR side pockets.[17] Given the similar BAS distribution in H-MOR-A and H-MOR-B (Table 1), it is not surprising that the preferred exchange sites for Cu^{2+} in the Cu-MOR-B series are also the Al sites located in the pore mouth of 8-MR pockets.

However, it should be noted that while in the Cu-MOR-A series about 0.7 BAS were consumed per Cu ion exchanged, it was approximately 0.9 with the Cu-MOR-B series. The ratio of 0.7 BAS/Cu in the activated sample has been explained by the location of a tricopper cluster stabilized by two Al tetrahedra.[17] Thus, the higher involvement of BAS per Cu^{2+} ion in Cu-MOR-B is a first indication for differences in the speciation of Cu ions compared to the A series.

^{27}Al MAS NMR spectra of Cu-MOR-B series shows a significant decrease of octahedral Al, associated with EFAl with increasing Cu concentration (Figure S4b). The decrease in intensity for the tetrahedral Al species is accompanied by a simultaneous line broadening due to the impact of paramagnetic Cu^{2+}. Integration of the peak area corresponding to tetrahedral Al showed that its concentration remained constant with Cu loading. The linear decrease of octahedral Al upon Cu exchange is, therefore, attributed to the formation of new NMR-silent Al or, alternatively, to the conversion from octahedral to tetrahedral coordination upon Cu introduction.

The quantification of Al species having a different coordination based solely on NMR spectroscopy is subject to uncertainties due to the paramagnetism of Cu^{2+}.[33,45,46] Therefore, we used Al K-edge XAS to determine and quantify Al in different coordinations. Figure 3 shows the XANES Al spectra for samples of Cu-MOR-B series. The broad peak at 1568 eV decreases with Cu loading. Because this peak is attributed to Al in octahedral coordination,[47] the changes in Al K-XANES with increasing Cu loadings are attributed to the gradual transformation of octahedral into tetrahedral Al.[24,47−49]

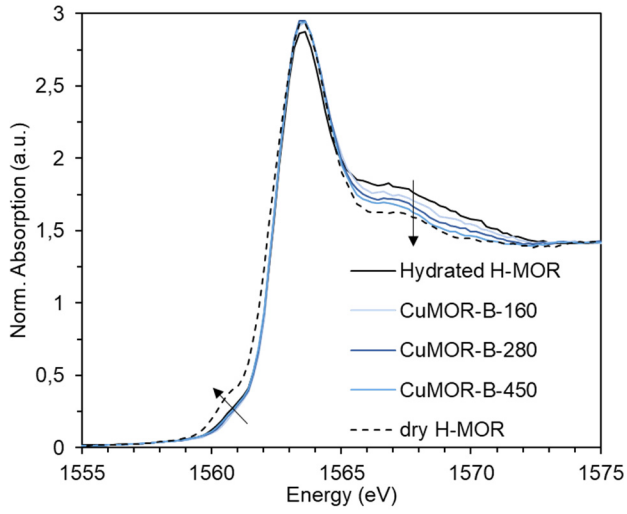

Figure 3. Al K-edge XANES of Cu-MOR-B series with different Cu loadings. Measurements were performed in hydrated states unless stated.

Linear combination fitting of XANES spectra was used to determine the concentration of tetrahedral and octahedral Al species. The spectra of dehydrated H-MOR-B was taken as a reference for 0% octahedral Al, since extra-framework Al

https://doi.org/10.1021/jacsau.1c00196
JACS Au 2021, 1, 1412−1421

changes its coordination from octahedral to tetrahedral upon losing water ligands. A small pre-edge feature at 1560.5 eV appeared with the dehydrated form of H-MOR-B sample due to the localization of H^+ at the negatively charged framework Al site, resulting from the loss of H_2O ligand molecules.[49] Hydrated H-MOR-B was used as a reference for octahedral Al quantification, with a concentration of 20% EFAl, as determined by ^{27}Al MAS NMR. It can be seen from Figure 4 that the concentration of octahedral Al decreased with

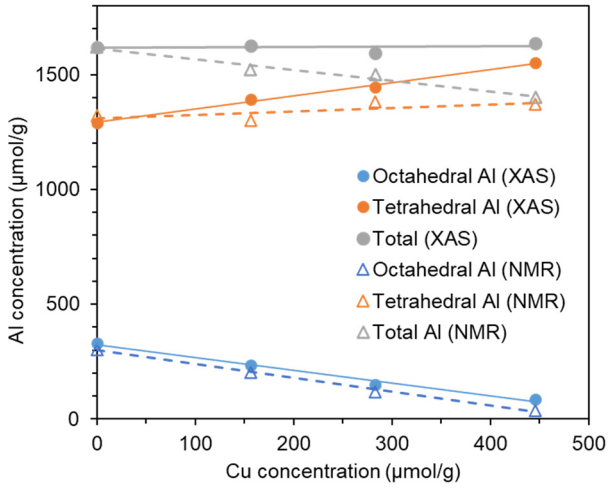

Figure 4. Concentration of tetrahedral, octahedral, and total Al of hydrated Cu-MOR-B series obtained by LCF of Al K-edge XANES (full symbols) and ^{27}Al NMR measured on a 500 MHz instrument (hollow symbols).

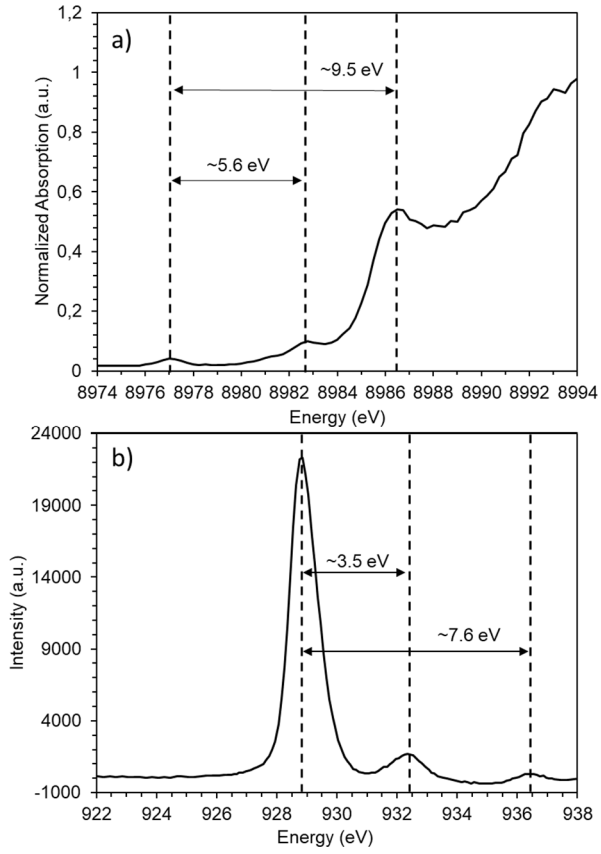

Figure 5. (a) Cu K-edge HERFD-XANES; (b) Cu L_3-edge XANES of Cu-MOR-B-280 activated in O_2 at 450 °C for 1 h.

increasing Cu concentration, in good agreement with ^{27}Al MAS NMR spectra (Figure 4, hollow symbols). The relative amount of tetrahedral Al linearly increased with increasing Cu concentration.

These results lead to the hypothesis that the direct interaction of octahedral Al with Cu^{2+} ions induces the change in Al coordination. In view of the calculated concentrations of octahedral Al by XAS and NMR, we conclude that the linear decrease of the octahedral fraction of Al is mainly due to the change in coordination upon interaction with Cu ions. In particular, concentrations obtained from Al XAS analysis (Figure 4) point to the reaction of about two Cu atoms with one Al. The specific interaction of Cu^{2+} with octahedral, that is, extra-framework, suggests the formation of tetrahedral Al, and of $CuAl_xO_y$ nanoclusters as a possible structure, with $x = 0.5$.

X-ray Absorption Spectroscopic Study of Highly Active Cu-MOR Species

In order to investigate a representative member of the Cu-MOR-B series, a sample with a Cu concentration of 283 μmol/g and a Cu_{eff} of 0.58 was selected for detailed XAS experimental studies in combination with computational studies.

Figure 5 shows the Cu K-edge and Cu L_3-edge X-ray absorption near edge structure (XANES) of O_2 activated Cu-MOR-B-280. The combined use of K- and L_3-edge XANES allows unambiguous determination of the coordination structure and environment of Cu. Using HERFD-XANES resolves spectral features in the Cu K edge (Figure 5a) that are not detectable using conventional XANES.[50−53] However, it must be noted that the peak heights are different between the two measurements. The Cu K-edge XANES spectrum is provided for comparison (Figure S5a) in the SI.

In Cu K-edge XANES the pre-edge peak at about 8977.3 eV is attributed to quadrupole allowed 1s to 3d transitions. The appearance of the pre-edge feature is an indicator that Cu species in this Cu-MOR material are predominantly Cu^{2+}. Between the pre-edge at 8977.3 eV and the peak at 8986.7 eV (ΔE = 9.5 eV), a peak appeared at about 8982.8 eV (ΔE = 5.6 eV; Figures 5a and S5a). The energy corresponds to the Cu^+ 1s to 4p transition and is hypothesized to indicate either presence of Cu^+ stabilized by the zeolite[14,15,41,50] or is caused by beam damage due to the larger X-ray dose in HERFD-XANES.[54,55] In either form, this cation would not be actively involved in CH_4 oxidation. Figure 5b shows the L_3-edge XANES of Cu-MOR-B-280 with the main peak at about 928.8 eV and distinct satellite peaks at about 932.4 and 936.5 eV.

Structural Assignment of Cu Species Using AIMD and Simulated K- and L_3-Edge XANES and EXAFS Spectra

After establishing that Al is part of the active site, 11 Cu−Al−oxo and Cu−oxo clusters have been explored by AIMD simulations. The cluster models studied and the snapshots extracted from AIMD trajectories are shown in Figure S6. AIMD simulations at 298 K with clusters and Al atoms at different sites are compiled in Figure S8. As Cu^{2+} has been established to be located in the 8-MR side pockets of MOR,[17,18,56,57] only clusters in that location were considered. For a tentative composition of Cu_2AlO_3, two configurations are considered, that is, one with the Al atom away from the MOR surface (Cu−Al−Cu) and another with Al near the surface (Al−Cu−Cu). Spin multiplicities were found only to have a

https://doi.org/10.1021/jacsau.1c00196
JACS Au 2021, 1, 1412−1421

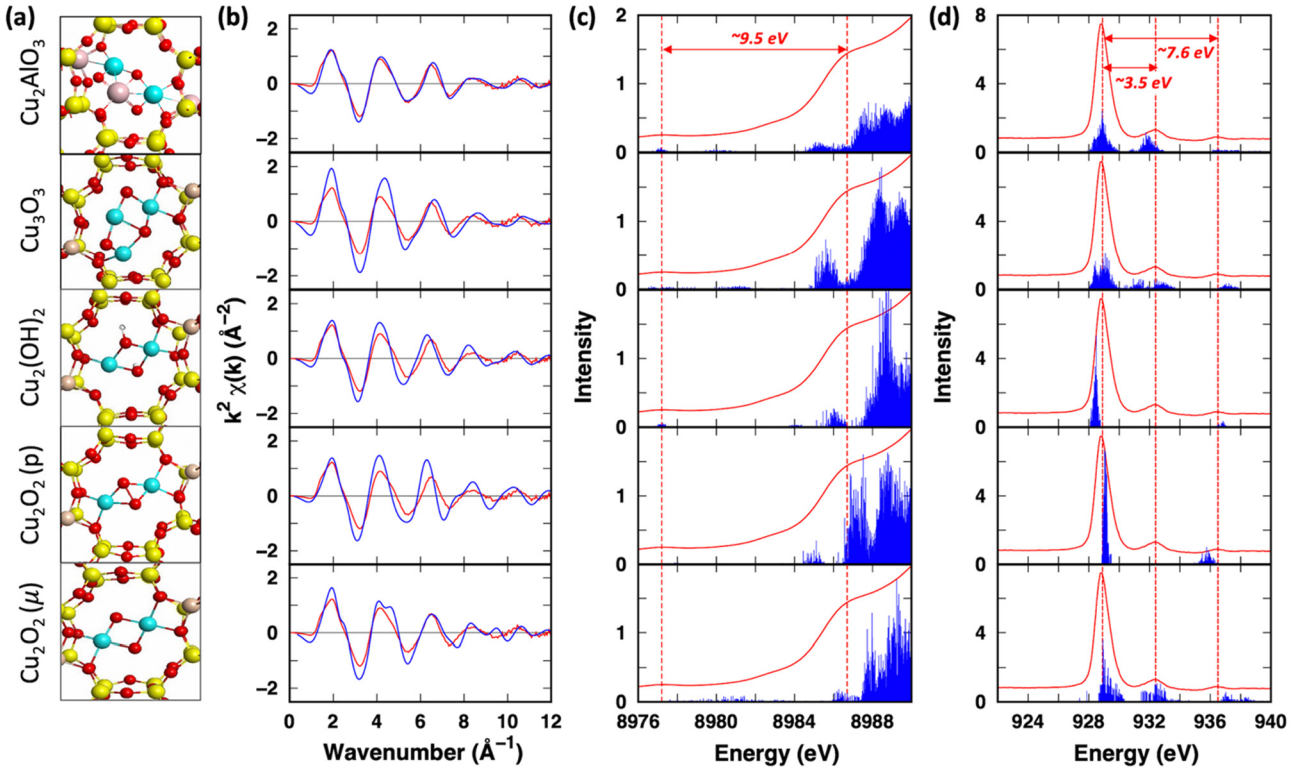

Figure 6. (a) Annealed structure, (b) compared k^2-weighted EXAFS ($k^2\chi(k)$) from calculation (blue line) and measurement (red lines), (c) K-edge XANES, and (d) L3-edge XANES spectra of selected systems. For spectra of the Cu trimer and Cu_2AlO_3, we plot ensemble averaged data with different Al and Cu cluster sites where individual spectra can be found in Figures S6 and S8. K-edge and L_3-edge XANES spectra are shifted by 88 and 2.1 eV, respectively, in order to match experimental pre-edge and main peak, and their intensities are with arbitrary units. (c) and (d) compare theoretical (blue lines) spectra with experimental ones (red line) along with red vertical guiding lines and energies, as shown in Figure 5a and b, respectively.

minor influence on the results. The simulated systems are listed in Table S3 of the SI. It should be emphasized at this point that the strength of the spectroscopic characterization and the associated modeling lies in the fact that three probes must yield agreement: XANES at the K- and the L_3-edge as well as the K-edge EXAFS. Only this combination provides now the ability of an unequivocal assignment, while each of the approaches alone would remain ambiguous, even when experiment and modeling are combined.

The comparison of both k- and R-space EXAFS simulated spectra with the experiments indicates that neither Cu monomers, nor mono-oxo and monohydroxo dicopper clusters or the Cu_2AlO_3 cluster with the Al−Cu−Cu configuration are likely structures. For these model clusters EXAFS simulations show large discrepancies with the experimental data obtained on the current samples in peak positions and intensities (Figure S8 in the SI). Figure 6a compiles snapshots of simulated structures having a reasonable agreement with the experiment. Figures 6 b and S10 show the averaged k- and R-space EXAFS, respectively, for these selected structures. In Figure 6c,d, we also show the corresponding ensemble averaged K-edge and L_3-edge XANES spectra. It should be noted that, for the Cu_3O_3 and Cu_2AlO_3 clusters in Figure 6, the spectra from S2−S4 sites were averaged (see Figures S8 and S10 in the SI that show the spectra for each site). This allows a reliable comparison with experimental spectra, which likely also represent an average of slightly different locations of the clusters.

Figure 6b clearly shows that the calculated $k^2\chi(k)$ EXAFS spectra of the Cu_2AlO_3 species agrees well with the experimental spectra. This can also be seen for the R-space (Figure S9a−c). The simulated spectra for Cu_3O_3 reproduce the positions of the first and second peaks very well, but show higher intensities than the experiment.

For the bis(μ-hydroxo) and peroxo dicopper systems, only the position and intensity of the first peak of $k^2\chi(k)$ EXAFS shows a good agreement with experimental data. The $k^2\chi(k)$ EXAFS of bis(μ-oxo) Cu dimer can be ruled out, therefore, as neither the intensity of the first peak nor the shape of the second peak is reproduced and also scattering above k = 8 Å^{-1} is poorly reproducing the experimental data (Figure S8). The detailed analysis of the EXAFS peaks and their relation to the structure are compiled in section S6 of the SI.

Analysis of K-edge and L_3-edge XANES simulated spectra offer further insight in the structure of the active species. Figure 6c,d shows the simulated XANES spectra with guiding lines added to facilitate comparisons of the calculated energy difference (ΔE) with the experimental values (Figure 5 and red line in Figure 6c,d). The simulated K-edge XANES spectra of Cu_2AlO_3, Cu_3O_3, and the bis(μ-oxo) and peroxo Cu_2O_2 clusters show a transition at ΔE greater than 10 eV, which is attributed to the dipole allowed 1s to 4p transition, but at higher energies than the experimental value of 9.5 eV (see Figure 5).

All simulated L_3-edge XANES spectra show a main peak at ~929 eV, corresponding to Cu^{2+} 2p to 3d dipole transitions, with distinct satellite features. Simulated L_3-edge XANES

https://doi.org/10.1021/jacsau.1c00196
JACS Au 2021, 1, 1412−1421

spectrum of Cu_2AlO_3 species shows transitions at ΔE = ~3.3 and ~7.8 eV, which agree well with the features observed at ΔE = ~3.5 and ~7.6 eV (Figure 5b). While the Cu_3O_3 structure shows a main peak and satellite peaks at ΔE values similar to the Cu_2AlO_3 structure, the additional peak at ΔE = ~2.0 eV has not been detected in the experiment, and the structure can be ruled out on this basis. For the bis(μ-hydroxo) and peroxo dimers, the satellite peak at ΔE = ~3.5 eV was not observed in simulated spectra. Interestingly, for the bis(μ-oxo) dimer, which is ruled out on the basis of the EXAFS calculations, the simulated spectra show energy differences similar to the experiment although with higher peak energies. Based on L_3-edge XANES, the spectra calculated for Cu_2AlO_3 is consistent with all experimental spectra and is, therefore, concluded to be the most likely structure causing the transformation of methane to methanol; see SI (section S7 and Figure S11) for further discussion. We conclude, therefore, that the activation of CH_4 in the highly efficient Cu-MOR materials is indeed performed by a Cu_2AlO_3 species, with the structure shown in Figure 6a, top. The data suggest that the formation of such Cu_2AlO_3 clusters requires the presence of extra-framework alumina at the bottom of the side pocket (i.e., not accessible for pyridine).

CONCLUSIONS

A series of Cu-MOR catalysts with an unprecedently high fraction of Cu being active in selective methane oxidation to methanol has been synthesized. The activity to form oxidized molecules in a stepwise reaction combined with characterization by NMR, IR, and X-ray absorption spectroscopy point to the formation of Cu−Al clusters in the 8-MR side pockets, linking exchanged Cu^{2+} species with extra-framework Al moieties that were originally located at the bottom of the side pocket of MOR.

The combined experiment and simulation of Cu K and L_3 XANES together with EXAFS spectra allows unequivocally identifying the oxide clusters to consist of two Cu atoms and one Al atom linked by oxygen (Figure 6a). This cluster is located in the side pocket and shows the ability to oxidize 1.2 methane molecules on average when exposed to 1 bar of methane. Therefore, the amount of CH_4 activated per Cu in these materials corresponds to the utilization of one to up to two O atoms per cluster, analogous to the variations in reactivity observed for μ-oxo species in Cu_3O_3 clusters with chemical potential.[22] However, we cannot unambiguously rule out the presence of a minority species, a highly active Cu−oxo cluster with Cu_{eff} > 0.5, that could also account for the excess of CH_4 activated.

At present, we can only speculate about the reason for the higher reactivity of the oxygen or the easier reducibility of Cu^{2+} in the $[Cu_2AlO_3]^{2+}$ cluster. One of the currently preferred hypotheses is that the distortion of the cluster decreases the stability of the Me−O bond strength. Detailed calculations on the chemical reactivity are currently being performed, but the discussion of these aspects is beyond the scope of the current paper.

EXPERIMENTAL AND COMPUTATIONAL METHODS

Preparation of Cu-MOR Samples

Commercial NH_4-MOR (Si/Al = 10 and 11) were purchased by Clariant, and the corresponding H-form was obtained after calcination in synthetic air (100 mL/min) at 550 °C (10 K/min) for 6 h. The H-MOR samples with Si/Al = 11 and 10 were denoted as H-MOR-A and H-MOR-B. Cu-MOR samples were prepared by aqueous ion exchange of H-MOR at ambient temperature in aqueous solutions of $Cu(CH_3COO)_2$ (Sigma-Aldrich, 99.99%) for 20 h. The pH of the solution was kept to 5.5−6.0 with during the Cu-exchange. Si, Al, Na, and Cu contents were measured by atomic absorption spectroscopy (AAS) on a UNICAM 939 AA spectrometer after dissolution in boiling hydrofluoric acid.

Activity Tests in Selective Oxidation of CH_4

The activity was tested under atmospheric pressure in a stainless steel plug flow reactor with a 4 mm inner diameter. In a typical reaction, 50 mg of Cu-MOR was first activated for 1 h in O_2 at 500 °C, cooled down to 200 °C, and then flushed with He. In the next step, 90% CH_4 in He was flown over the sample for 4 h. The samples were then cooled to 135 °C in He and a steam-assisted product desorption was performed with 50% H_2O in He. Reaction products were identified and quantified with online mass spectroscopy by monitoring the m/z signals of 31, 44, and 46 for CH_3OH, CO_2, and $(CH_3)_2O$, respectively.

In Situ Infrared (IR) Spectroscopy

The samples for IR spectroscopy were pressed as self-supporting wafers with a density of about 10 mg/cm^2 and activated in vacuum (1.0×10^{-7} mbar) at 450 °C with a heating rate of 10 K/min for 1 h. IR spectroscopy of pyridine adsorption were measured on Thermo Nicolet 5700 FT-IR spectrometer with a resolution of 4 cm^{-1}. The measurements were performed before and after pyridine adsorption at 150 °C.

^{27}Al Magic-Angle Spinning (MAS) Nuclear Magnetic Resonance (NMR) Spectroscopy

^{27}Al MAS NMR spectra were recorded on a Bruker Avance 500 Ultrashield NMR spectrometer with a magnetic field of 11.75 T corresponding to the Lamor frequency of 130.3 MHz and the rotor was spun at 12 kHz. 2400 spectra were accumulated in a single pulse sequence with a pulse width of 1.16 μs and the relaxation delay of 2 s. Parent H-MOR zeolites were measured on a Varian-Agilent Inova 63 mm wide-bore 900 MHz NMR spectrometer. The samples were packed in a 3.2 mm pencil type MAS probe with a magnetic field of 21.1 T, corresponding to the Lamor frequency of 234.56 MHz and the rotor was spun at 20 kHz. A total of 5000 scans were recorded in a single pulse sequence with a pulse length of 2.0 μs and relaxation delay of 1 s.

Al K-Edge and Cu L-Edge XAFS

X-ray absorption spectra at Al K-edge and Cu L-edge spectra were measured at the Swiss Light Source (SLS) of the Paul Scherrer Institut (Villigen, Swiss) on PHOENIX II. All measurements were carried out in fluorescence mode. X-ray fluorescence signal was detected by an one-element energy dispersive Silicon drift diode (DSS, manufacturer KeteK, Germany). The introduced gases were further dried by using Supelco 5A Moisture trap. ATHENA software was used during the background processing. XANES normalization follows standard protocol used within the Athena software.[58]

Cu K-Edge XANES

HERFD XANES measurements were carried on beamline P64 at PETRA III of DESY (Hamburg, Germany). Conventional Cu K-edge XANES measurements were carried out on beamline P65 at PETRA III of DESY in Hamburg, Germany. A double-crystal Si(111) monochromator was used to control the incident photon energy, and the spectra were recorded with ionization chamber detectors in the transmission mode. The gases were further dried by using Supelco 5A Moisture trap. ATHENA software was used during the background processing. XANES normalization follows standard protocol used within the Athena software.[58]

Further details of the experimental methods are provided in the section S1 of the Supporting Information.

https://doi.org/10.1021/jacsau.1c00196
JACS Au 2021, 1, 1412−1421

DFT Calculations

Periodic spin-polarized density functional theory (DFT) calculations are performed within the generalized gradient approximation (GGA) with the exchange correlation functional of Perdew, Burke, and Ernzerhoff (PBE)[59] as implemented in the CP2K package.[60,61] Grimme's third-generation corrections (DFT-D3) are used to take into account dispersion forces or van der Waals interactions to describe energies more precisely.[62] For the core electrons, Goedecker−Teter−Hutter (GTH) pseudopotentials are used,[63] while the valence wave functions are expanded in terms of double-ζ quality basis sets optimized for condensed systems to minimize linear dependencies and superposition errors.[64] Electrostatic terms are calculated using an additional auxiliary plane-wave basis set with a 400 Ry cutoff. The Γ-point approximation is employed for the Brillouin zone integration because of the significant size of the supercell.

AIMD Simulations. Starting with a cell-optimized mordenite supercell, DFT-based ab initio molecular dynamics (AIMD) simulations are performed within the canonical NVT ensemble at room temperature using a1.0 fs time step and a Nosé−Hoover chain thermostat with a frequency of 1500 cm^{-1} to control the temperature to determine the local structure and their dynamic properties. We considered the different spin multiplicities for each system. For each simulation, well-equilibrated trajectories of ≥35 ps were collected to obtain reliable statistical properties.

EXAFS Simulations. We simulated K-edge EXAFS spectra with FEFF8.5 program[65] using ≥500 snapshots extracted from NVT trajectories with equally spaced by ∼0.05 ps for each system. For each system, each snapshot was used to calculate a full set of scattering (single and multiple scattering) paths for all atoms within 6.5 Å of each Cu site using FEFF8.5 program.[65]

XANES Calculations with Time-Dependent DFT. Excited-state XANES calculations were performed at the Cu K- and L_3-edge for selected systems screened from a comparison of experimental and simulated XANES spectra using a TDDFT-based restricted excitation window approach,[66,67] as implemented in the NWChem quantum chemistry program.[66,68] All calculated spectra were Lorentzian-broadened by 0.6. The ensemble averaged TDDFT XANES spectra were generated from >50 structures that were equally spaced by 0.5 ps.

Further details of the computational methods are provided in section S4 of the Supporting Information.

■ ASSOCIATED CONTENT

Supporting Information

The Supporting Information is available free of charge at https://pubs.acs.org/doi/10.1021/jacsau.1c00196.

S1: Materials and experimental methods; S2: Additional activity results; S3: Characterization of parent MOR zeolites and Cu-MOR series; S4: Computational details; S5: Structural changes during AIMD simulations; S6: A detailed analysis of the EXAFS peaks and their relation to the structure; S7: Tri-coordinated Cu on Cu_2AlO_3; S8: Coordinates of annealed structures; Supplementary references (PDF)

■ AUTHOR INFORMATION

Corresponding Authors

Johannes A. Lercher − *Department of Chemistry and Catalysis Research Center, TU München, 85748 Garching, Germany; Institute for Integrated Catalysis, Pacific Northwest National Laboratory, Richland, Washington 99354, United States;* orcid.org/0000-0002-2495-1404; Email: johannes.lercher@pnnl.gov

Maricruz Sanchez-Sanchez − *Department of Chemistry and Catalysis Research Center, TU München, 85748 Garching, Germany;* orcid.org/0000-0002-3769-9623; Email: m.sanchez@tum.de

Mal-Soon Lee − *Institute for Integrated Catalysis, Pacific Northwest National Laboratory, Richland, Washington 99354, United States;* orcid.org/0000-0001-6851-177X; Email: malsoon.lee@pnnl.gov

Authors

Insu Lee − *Department of Chemistry and Catalysis Research Center, TU München, 85748 Garching, Germany*

Lei Tao − *Department of Chemistry and Catalysis Research Center, TU München, 85748 Garching, Germany*

Takaaki Ikuno − *Department of Chemistry and Catalysis Research Center, TU München, 85748 Garching, Germany*

Rachit Khare − *Department of Chemistry and Catalysis Research Center, TU München, 85748 Garching, Germany;* orcid.org/0000-0002-1519-5184

Andreas Jentys − *Department of Chemistry and Catalysis Research Center, TU München, 85748 Garching, Germany;* orcid.org/0000-0001-5877-5042

Thomas Huthwelker − *Swiss Light Source, Laboratory for Synchrotron Radiation and Femtochemistry (LSF), 5232 Villigen, Switzerland*

Camelia N. Borca − *Swiss Light Source, Laboratory for Synchrotron Radiation and Femtochemistry (LSF), 5232 Villigen, Switzerland*

Aleksandr Kalinko − *Photon Science DESY, 22607 Hamburg, Germany*

Oliver Y. Gutiérrez − *Institute for Integrated Catalysis, Pacific Northwest National Laboratory, Richland, Washington 99354, United States*

Niri Govind − *Physical Sciences Division, Pacific Northwest National Laboratory, Richland, Washington 99354, United States;* orcid.org/0000-0003-3625-366X

John L. Fulton − *Institute for Integrated Catalysis, Pacific Northwest National Laboratory, Richland, Washington 99354, United States;* orcid.org/0000-0001-9361-9803

Jian Zhi Hu − *Institute for Integrated Catalysis, Pacific Northwest National Laboratory, Richland, Washington 99354, United States;* orcid.org/0000-0001-8879-747X

Vassiliki-Alexandra Glezakou − *Institute for Integrated Catalysis, Pacific Northwest National Laboratory, Richland, Washington 99354, United States;* orcid.org/0000-0001-6028-7021

Roger Rousseau − *Institute for Integrated Catalysis, Pacific Northwest National Laboratory, Richland, Washington 99354, United States;* orcid.org/0000-0003-1947-0478

Complete contact information is available at: https://pubs.acs.org/10.1021/jacsau.1c00196

Author Contributions

†These authors contributed equally to this work.

Notes

The authors declare no competing financial interest.

■ ACKNOWLEDGMENTS

I.L., T.I., L.T., M.S.-S., and J.A.L. are thankful to the Deutsche Forschungsgemeinschaft (DFG, Project Number 326562156) and the TUM International Graduate School of Science and Engineering (IGSSE) for financial support. M.-S.L., O.Y.G., J.L.F., J.Z.H., V.-A.G., R.R., and J.A.L. were supported by the U.S. Department of Energy (DOE), Office of Science, Office of

Basic Energy Sciences, Division of Chemical Sciences, Geosciences and Biosciences (Transdisciplinary Approaches to Realize Novel Catalytic Pathways to Energy Carriers, FWP 47319). Computational work was performed using the Molecular Sciences Computing Facility (MSCF) in the William R. Wiley Environmental Molecular Sciences Laboratory, a U.S. Department of Energy (DOE) national scientific user facility sponsored by the DOE's Office of Biological and Environmental Research and located and the Pacific Northwest National Laboratory (PNNL) and the National Energy Research Scientific Computing Center (NERSC) located at Lawrence Berkley National Laboratory provided by a user proposal. PNNL is operated by Battelle for DOE. We acknowledge DESY beamlines P-64 and P-65 (Hamburg, Germany), a member of the Helmholtz Association HGF, for the provision of experimental facilities for X-ray experiments. The used infrastructure of the von Hamos spectrometer at the beamline P64 was realized in the frame of Projects FKZ 05K13UK1 and FKZ 05K14PP1. A.J. and R.K. were supported by BMBF under Project MatDynamics (Verbundprojekt 05K13W03). We acknowledge the Paul Scherrer Institut, Villigen, Switzerland, for the provision of synchrotron beamtime at beamline PHOENIX of the SLS. The authors thank Matthias Bauer for his assistance.

REFERENCES

(1) Caballero, A.; Perez, P. J. Methane as raw material in synthetic chemistry: the final frontier. *Chem. Soc. Rev.* **2013**, *42*, 8809−8820.
(2) Alvarez-Galvan, M. C.; Mota, N.; Ojeda, M.; Rojas, S.; Navarro, R. M.; Fierro, J. L. G. Direct methane conversion routes to chemicals and fuels. *Catal. Today* **2011**, *171*, 15−23.
(3) Newton, M. A.; Knorpp, A. J.; Sushkevich, V. L.; Palagin, D.; van Bokhoven, J. A. Active sites and mechanisms in the direct conversion of methane to methanol using Cu in zeolitic hosts: a critical examination. *Chem. Soc. Rev.* **2020**, *49*, 1449−1486.
(4) Malakoff, D. The gas surge. *Science* **2014**, *344*, 1464.
(5) Olah, G. A. Beyond Oil and Gas: The Methanol Economy. *Angew. Chem., Int. Ed.* **2005**, *44*, 2636−2639.
(6) Ma, Y.; Cheng, S.; Wu, X.; Shi, Y.; Cao, L.; Liu, L.; Ran, R.; Si, Z.; Liu, J.; Weng, D. Low-Temperature Solid-State Ion-Exchange Method for Preparing Cu-SSZ-13 Selective Catalytic Reduction Catalyst. *ACS Catal.* **2019**, *9*, 6962−6973.
(7) Ravi, M.; Ranocchiari, M.; van Bokhoven, J. A. The Direct Catalytic Oxidation of Methane to Methanol—A Critical Assessment. *Angew. Chem., Int. Ed.* **2017**, *56*, 16464−16483.
(8) Groothaert, M. H.; van Bokhoven, J. A.; Battiston, A. A.; Weckhuysen, B. M.; Schoonheydt, R. A. Bis(μ-oxo)dicopper in Cu-ZSM-5 and Its Role in the Decomposition of NO: A Combined in Situ XAFS, UV-Vis-Near-IR, and Kinetic Study. *J. Am. Chem. Soc.* **2003**, *125*, 7629−7640.
(9) Park, M. B.; Ahn, S. H.; Mansouri, A.; Ranocchiari, M.; van Bokhoven, J. A. Comparative Study of Diverse Copper Zeolites for the Conversion of Methane into Methanol. *ChemCatChem* **2017**, *9*, 3705−3713.
(10) Groothaert, M. H.; Smeets, P. J.; Sels, B. F.; Jacobs, P. A.; Schoonheydt, R. A. Selective Oxidation of Methane by the Bis(μ-oxo)dicopper Core Stabilized on ZSM-5 and Mordenite Zeolites. *J. Am. Chem. Soc.* **2005**, *127*, 1394−1395.
(11) Alayon, E. M. C.; Nachtegaal, M.; Bodi, A.; Ranocchiari, M.; van Bokhoven, J. A. Bis(μ-oxo) versus mono(μ-oxo)dicopper cores in a zeolite for converting methane to methanol: an in situ XAS and DFT investigation. *Phys. Chem. Chem. Phys.* **2015**, *17*, 7681−7693.
(12) Alayon, E. M. C.; Nachtegaal, M.; Bodi, A.; van Bokhoven, J. A. Reaction conditions of methane-to-methanol conversion affect the structure of active copper sites. *ACS Catal.* **2014**, *4*, 16−22.
(13) Vanelderen, P.; Snyder, B. E. R.; Tsai, M.-L.; Hadt, R. G.; Vancauwenbergh, J.; Coussens, O.; Schoonheydt, R. A.; Sels, B. F.; Solomon, E. I. Spectroscopic Definition of the Copper Active Sites in Mordenite: Selective Methane Oxidation. *J. Am. Chem. Soc.* **2015**, *137*, 6383−6392.
(14) Brezicki, G.; Kammert, J. D.; Gunnoe, T. B.; Paolucci, C.; Davis, R. J. Insights into the Speciation of Cu in the Cu-H-Mordenite Catalyst for the Oxidation of Methane to Methanol. *ACS Catal.* **2019**, *9*, 5308−5319.
(15) Pappas, D. K.; Martini, A.; Dyballa, M.; Kvande, K.; Teketel, S.; Lomachenko, K. A.; Baran, R.; Glatzel, P.; Arstad, B.ør.; Berlier, G.; Lamberti, C.; Bordiga, S.; Olsbye, U.; Svelle, S.; Beato, P.; Borfecchia, E. The Nuclearity of the Active Site for Methane to Methanol Conversion in Cu-Mordenite: A Quantitative Assessment. *J. Am. Chem. Soc.* **2018**, *140*, 15270−15278.
(16) Ikuno, T.; Grundner, S.; Jentys, A.; Li, G.; Pidko, E.; Fulton, J.; Sanchez-Sanchez, M.; Lercher, J. A. Formation of Active Cu-oxo Clusters for Methane Oxidation in Cu-Exchanged Mordenite. *J. Phys. Chem. C* **2019**, *123*, 8759−8769.
(17) Grundner, S.; Markovits, M. A.C.; Li, G.; Tromp, M.; Pidko, E. A.; Hensen, E. J.M.; Jentys, A.; Sanchez-Sanchez, M.; Lercher, J. A. Single-site trinuclear copper oxygen clusters in mordenite for selective conversion of methane to methanol. *Nat. Commun.* **2015**, *6*, 7546.
(18) Grundner, S.; Luo, W.; Sanchez-Sanchez, M.; Lercher, J. A. Synthesis of single-site copper catalysts for methane partial oxidation. *Chem. Commun.* **2016**, *52*, 2553−2556.
(19) Kim, Y.; Kim, T. Y.; Lee, H.; Yi, J. Distinct activation of Cu-MOR for direct oxidation of methane to methanol. *Chem. Commun.* **2017**, *53*, 4116−4119.
(20) Latimer, A. A.; Kulkarni, A. R.; Aljama, H.; Montoya, J. H.; Yoo, J. S.; Tsai, C.; Abild-Pedersen, F.; Studt, F.; Nørskov, J. K. Understanding trends in C-H bond activation in heterogeneous catalysis. *Nat. Mater.* **2017**, *16*, 225−229.
(21) Snyder, B. E. R.; Vanelderen, P.; Schoonheydt, R. A.; Sels, B. F.; Solomon, E. I. Second-Sphere Effects on Methane Hydroxylation in Cu-Zeolites. *J. Am. Chem. Soc.* **2018**, *140*, 9236−9243.
(22) Zheng, J.; Lee, I.; Khramenkova, E.; Wang, M.; Peng, B.; Gutierrez, O. Y.; Fulton, J. L.; Camaioni, D. M.; Khare, R.; Jentys, A.; Haller, G. L.; Pidko, E. A.; Sanchez-Sanchez, M.; Lercher, J. A. Importance of Methane Chemical Potential for Its Conversion to Methanol on Cu-Exchanged Mordenite. *Chem. - Eur. J.* **2020**, *26*, 7563−7567.
(23) Xu, B.; Rotunno, F.; Bordiga, S.; Prins, R.; van Bokhoven, J. A. Reversibility of structural collapse in zeolite Y: Alkane cracking and characterization. *J. Catal.* **2006**, *241*, 66−73.
(24) van Bokhoven, J. A.; van der Eerden, A. M. J.; Koningsberger, D. C. Three-Coordinate Aluminum in Zeolites Observed with In situ X-ray Absorption Near-Edge Spectroscopy at the Al K-Edge: Flexibility of Aluminum Coordinations in Zeolites. *J. Am. Chem. Soc.* **2003**, *125*, 7435−7442.
(25) Yu, Z.; Zheng, A.; Wang, Q.; Chen, L.; Xu, J.; Amoureux, J.-P.; Deng, F. Insights into the Dealumination of Zeolite HY Revealed by Sensitivity-Enhanced 27Al DQ-MAS NMR Spectroscopy at High Field. *Angew. Chem., Int. Ed.* **2010**, *49*, 8657−8661.
(26) van Bokhoven, J. A.; Koningsberger, D. C.; Kunkeler, P.; van Bekkum, H.; Kentgens, A. P. M. Stepwise Dealumination of Zeolite Beta at Specific T-Sites Observed with 27Al MAS and 27Al MQ MAS NMR. *J. Am. Chem. Soc.* **2000**, *122*, 12842−12847.
(27) Agostini, G.; Lamberti, C.; Palin, L.; Milanesio, M.; Danilina, N.; Xu, B.; Janousch, M.; van Bokhoven, J. A. In Situ XAS and XRPD Parametric Rietveld Refinement To Understand Dealumination of Y Zeolite Catalyst. *J. Am. Chem. Soc.* **2010**, *132*, 667−678.
(28) Yi, X.; Liu, K.; Chen, W.; Li, J.; Xu, S.; Li, C.; Xiao, Y.; Liu, H.; Guo, X.; Liu, S.-B.; Zheng, A. Origin and Structural Characteristics of Tri-coordinated Extra-framework Aluminum Species in Dealuminated Zeolites. *J. Am. Chem. Soc.* **2018**, *140*, 10764−10774.
(29) Liu, C.; Li, G.; Hensen, E. J. M.; Pidko, E. A. Relationship between acidity and catalytic reactivity of faujasite zeolite: A periodic DFT study. *J. Catal.* **2016**, *344*, 570−577.

https://doi.org/10.1021/jacsau.1c00196
JACS Au 2021, 1, 1412−1421

(30) Schallmoser, S.; Ikuno, T.; Wagenhofer, M. F.; Kolvenbach, R.; Haller, G. L.; Sanchez-Sanchez, M.; Lercher, J. A. Impact of the local environment of Brønsted acid sites in ZSM-5 on the catalytic activity in n-pentane cracking. *J. Catal.* **2014**, *316*, 93−102.
(31) van Bokhoven, J. A.; Tromp, M; Koningsberger, D. C.; Miller, J. T.; Pieterse, J. A. Z.; Lercher, J. A.; Williams, B. A.; Kung, H. H. An Explanation for the Enhanced Activity for Light Alkane Conversion in Mildly Steam Dealuminated Mordenite: The Dominant Role of Adsorption. *J. Catal.* **2001**, *202*, 129−140.
(32) Liu, C.; Li, G.; Hensen, E. J. M.; Pidko, E. A. Nature and Catalytic Role of Extraframework Aluminum in Faujasite Zeolite: A Theoretical Perspective. *ACS Catal.* **2015**, *5*, 7024−7033.
(33) Dyballa, M.; Pappas, D. K.; Kvande, K.; Borfecchia, E.; Arstad, B.ør.; Beato, P.; Olsbye, U.; Svelle, S. On How Copper Mordenite Properties Govern the Framework Stability and Activity in the Methane-to-Methanol Conversion. *ACS Catal.* **2019**, *9*, 365−375.
(34) Hämäläinen, K.; Siddons, D. P.; Hastings, J. B.; Berman, L. E. Elimination of the inner-shell lifetime broadening in x-ray-absorption spectroscopy. *Phys. Rev. Lett.* **1991**, *67*, 2850−2853.
(35) Qayyum, M. F.; Sarangi, R.; Fujisawa, K.; Stack, T. D. P.; Karlin, K. D.; Hodgson, K. O.; Hedman, B.; Solomon, E. I. L-Edge X-ray Absorption Spectroscopy and DFT Calculations on Cu_2O_2 Species: Direct Electrophilic Aromatic Attack by Side-on Peroxo Bridged Dicopper(II) Complexes. *J. Am. Chem. Soc.* **2013**, *135*, 17417−17431.
(36) Aprà, E.; Bylaska, E. J.; de Jong, W. A.; Govind, N.; Kowalski, K.; Straatsma, T. P.; Harrison, R. J.; et al. NWChem: Past, present, and future. *J. Chem. Phys.* **2020**, *152*, 184102.
(37) Tao, L.; Lee, I.; Sanchez-Sanchez, M. Cu oxo nanoclusters for direct oxidation of methane to methanol: formation, structure and catalytic performance. *Catal. Sci. Technol.* **2020**, *10*, 7124−7141.
(38) Dedecek, J.; Kaucky, D.; Wichterlova, B.; Gonsiorova, O. Co2+ ions as probes of Al distribution in the framework of zeolites. ZSM-5 study. *Phys. Chem. Chem. Phys.* **2002**, *4*, 5406−5413.
(39) Dědeček, J.; Sobalík, Z.; Wichterlová, B. Siting and Distribution of Framework Aluminium Atoms in Silicon-Rich Zeolites and Impact on Catalysis. *Catal. Rev.: Sci. Eng.* **2012**, *54*, 135−223.
(40) Markovits, M. A. C.; Jentys, A.; Tromp, M.; Sanchez-Sanchez, M.; Lercher, J. A. Effect of Location and Distribution of Al Sites in ZSM-5 on the Formation of Cu-Oxo Clusters Active for Direct Conversion of Methane to Methanol. *Top. Catal.* **2016**, *59*, 1554−1563.
(41) Pappas, D. K.; Borfecchia, E.; Dyballa, M.; Pankin, I. A.; Lomachenko, K. A.; Martini, A.; Signorile, M.; Teketel, S.; Arstad, B.ør.; Berlier, G.; Lamberti, C.; Bordiga, S.; Olsbye, U.; Lillerud, K. P.; Svelle, S.; Beato, P. Methane to Methanol: Structure-Activity Relationships for Cu-CHA. *J. Am. Chem. Soc.* **2017**, *139*, 14961−14975.
(42) Eder, F.; Stockenhuber, M.; Lercher, J. A. Brønsted Acid Site and Pore Controlled Siting of Alkane Sorption in Acidic Molecular Sieves. *J. Phys. Chem. B* **1997**, *101*, 5414−5419.
(43) Triantafillidis, C. S.; Vlessidis, A. G.; Evmiridis, N. P. Dealuminated H-Y Zeolites: Influence of the Degree and the Type of Dealumination Method on the Structural and Acidic Characteristics of H-Y Zeolites. *Ind. Eng. Chem. Res.* **2000**, *39*, 307−319.
(44) Veefkind, V. A.; Smidt, M. L.; Lercher, J. A. On the role of strength and location of Brønsted acid sites for ethylamine synthesis on mordenite catalysts. *Appl. Catal., A* **2000**, *194*−*195*, 319−332.
(45) Kwak, J. H.; Tran, D.; Burton, S. D.; Szanyi, J.; Lee, J. H.; Peden, C. H. F. Effects of hydrothermal aging on NH3-SCR reaction over Cu/zeolites. *J. Catal.* **2012**, *287*, 203−209.
(46) Beale, A. M.; Gao, F.; Lezcano-Gonzalez, I.; Peden, C. H. F.; Szanyi, J. Recent advances in automotive catalysis for NOx emission control by small-pore microporous materials. *Chem. Soc. Rev.* **2015**, *44*, 7371−7405.
(47) Drake, I. J.; Zhang, Y.; Gilles, M. K.; Teris Liu, C. N.; Nachimuthu, P.; Perera, R. C. C.; Wakita, H.; Bell, A. T. An In Situ Al K-Edge XAS Investigation of the Local Environment of H+- and Cu+-Exchanged USY and ZSM-5 Zeolites. *J. Phys. Chem. B* **2006**, *110*, 11665−11676.
(48) Bugaev, L. A.; van Bokhoven, J. A.; Sokolenko, A. P.; Latokha, Y. V.; Avakyan, L. A. Local Structure of Aluminum in Zeolite Mordenite as Affected by Temperature. *J. Phys. Chem. B* **2005**, *109*, 10771−10778.
(49) Vjunov, A.; Wang, M.; Govind, N.; Huthwelker, T.; Shi, H.; Mei, D.; Fulton, J. L.; Lercher, J. A. Tracking the Chemical Transformations at the Brønsted Acid Site upon Water-Induced Deprotonation in a Zeolite Pore. *Chem. Mater.* **2017**, *29*, 9030−9042.
(50) Alayon, E. M. C.; Nachtegaal, M.; Kleymenov, E.; van Bokhoven, J. A. Determination of the electronic and geometric structure of Cu sites during methane conversion over Cu-MOR with X-ray absorption spectroscopy. *Microporous Mesoporous Mater.* **2013**, *166*, 131−136.
(51) Günter, T.; Doronkin, D. E.; Carvalho, H. W. P.; Casapu, M.; Grunwaldt, J. D. HERFD-XANES and XES as complementary operando tools for monitoring the structure of Cubased zeolite catalysts during NOx-removal by ammonia SCR. *J. Phys.: Conf. Ser.* **2016**, *712*, 012071.
(52) Borfecchia, E.; Lomachenko, K. A.; Giordanino, F.; Falsig, H.; Beato, P.; Soldatov, A. V.; Bordiga, S.; Lamberti, C. Revisiting the nature of Cu sites in the activated Cu-SSZ-13 catalyst for SCR reaction. *Chem. Sci.* **2015**, *6*, 548−563.
(53) Pappas, D. K.; Borfecchia, E.; Dyballa, M.; Lomachenko, K. A.; Martini, A.; Berlier, G.; Arstad, B.ør.; Lamberti, C.; Bordiga, S.; Olsbye, U.; Svelle, S.; Beato, P. Understanding and Optimizing the Performance of Cu-FER for The Direct CH4 to CH3OH Conversion. *ChemCatChem* **2019**, *11*, 621−627.
(54) Bauer, M. HERFD-XAS and valence-to-core-XES: new tools to push the limits in research with hard X-rays? *Phys. Chem. Chem. Phys.* **2014**, *16*, 13827−13837.
(55) Lafuerza, S.; Retegan, M.; Detlefs, B.; Chatterjee, R.; Yachandra, V.; Yano, J.; Glatzel, P. New reflections on hard X-ray photon-in/photon-out spectroscopy. *Nanoscale* **2020**, *12*, 16270−16284.
(56) Palagin, D.; Knorpp, A. J.; Pinar, A. B.; Ranocchiari, M.; van Bokhoven, J. A. Assessing the relative stability of copper oxide clusters as active sites of a CuMOR zeolite for methane to methanol conversion: size matters? *Nanoscale* **2017**, *9*, 1144−1153.
(57) Kulkarni, A. R.; Zhao, Z.-J.; Siahrostami, S.; Nørskov, J. K.; Studt, F. Monocopper Active Site for Partial Methane Oxidation in Cu-Exchanged 8MR Zeolites. *ACS Catal.* **2016**, *6*, 6531−6536.
(58) Ravel, B.; Newville, M. ATHENA, ARTEMIS, HEPHAESTUS: data analysis for X-ray absorption spectroscopy using IFEFFIT. *J. Synchrotron Radiat.* **2005**, *12*, 537−541.
(59) Perdew, J. P.; Burke, K.; Ernzerhof, M. Generalized Gradient Approximation Made Simple. *Phys. Rev. Lett.* **1996**, *77*, 3865−3868.
(60) Kühne, T. D.; Iannuzzi, M.; Del Ben, M.; Rybkin, V. V.; Seewald, P.; Stein, F.; Hutter, J.; et al. CP2K: An electronic structure and molecular dynamics software package - Quickstep: Efficient and accurate electronic structure calculations. *J. Chem. Phys.* **2020**, *152*, 194103.
(61) VandeVondele, J.; Krack, M.; Mohamed, F.; Parrinello, M.; Chassaing, T.; Hutter, J. Quickstep: Fast and accurate density functional calculations using a mixed Gaussian and plane waves approach. *Comput. Phys. Commun.* **2005**, *167*, 103−128.
(62) Grimme, S.; Antony, J.; Ehrlich, S.; Krieg, H. A consistent and accurate ab initio parametrization of density functional dispersion correction (DFT-D) for the 94 elements H-Pu. *J. Chem. Phys.* **2010**, *132*, 154104.
(63) Goedecker, S.; Teter, M.; Hutter, J. Separable dual-space Gaussian pseudopotentials. *Phys. Rev. B: Condens. Matter Mater. Phys.* **1996**, *54*, 1703−1710.
(64) VandeVondele, J.; Hutter, J. Gaussian basis sets for accurate calculations on molecular systems in gas and condensed phases. *J. Chem. Phys.* **2007**, *127*, 114105.
(65) Ankudinov, A. L.; Ravel, B.; Rehr, J. J.; Conradson, S. D. Real-space multiple-scattering calculation and interpretation of x-ray-

https://doi.org/10.1021/jacsau.1c00196
JACS Au 2021, 1, 1412−1421

absorption near-edge structure. *Phys. Rev. B: Condens. Matter Mater. Phys.* **1998**, *58*, 7565−7576.
(66) Valiev, M.; Bylaska, E.J.; Govind, N.; Kowalski, K.; Straatsma, T.P.; Van Dam, H.J.J.; Wang, D.; Nieplocha, J.; Apra, E.; Windus, T.L.; de Jong, W.A. NWChem: A comprehensive and scalable open-source solution for large scale molecular simulations. *Comput. Phys. Commun.* **2010**, *181*, 1477−1489.
(67) Lopata, K.; Van Kuiken, B. E.; Khalil, M.; Govind, N. Linear-Response and Real-Time Time-Dependent Density Functional Theory Studies of Core-Level Near-Edge X-Ray Absorption. *J. Chem. Theory Comput.* **2012**, *8*, 3284−3292.
(68) Henkelman, G.; Arnaldsson, A.; Jónsson, H. A fast and robust algorithm for Bader decomposition of charge density. *Comput. Mater. Sci.* **2006**, *36*, 354−360.

https://doi.org/10.1021/jacsau.1c00196
JACS Au 2021, 1, 1412−1421